



CFD simulation of the effect of membrane thickness and reactants flow rate on water management in PEM fuel cells

Alessandro d'Adamo^{*} , Lorenzo Martocchia, Federico Croci , Carmine Marra 

Dipartimento di Ingegneria "Enzo Ferrari", Università degli Studi di Modena e Reggio Emilia, Modena, Italy

ARTICLE INFO

Keywords:

3D-CFD simulation of polymeric exchange membrane fuel cells
Improved self-humidification for thin membrane PEMFCs and low flow rate operation
Index for dominant water transport mode in the membrane
Index for self-humidification degree of the membrane

ABSTRACT

Polymeric Electrolyte Membrane Fuel Cells (PEMFCs) are receiving a higher-than-ever interest to maximize their specific performance and reach the industrial maturity for large-scale application. One of the most promising development directions consists in using ultra-thin electrolytes, which are known to lower the ohmic overpotential. However, thin membranes effects extend largely beyond the mere internal resistance reduction, encompassing the often-overlooked full spectrum of water-related processes and of species crossover.

In this study a three-dimensional multi-phase computational fluid dynamics (CFD) simulation model is presented and used to characterize the coupled current/water transport for two membrane thicknesses (30 and 6 μm), using experimental data from literature at high stoichiometry for model validation and extending the simulations to low flow rates corresponding to realistic stoichiometry. The simulation results highlight the complexity of the transport processes involved, resulting in a promoted self-humidification for thin membranes and under low stoichiometry. Two original figures of merit are introduced to (i) quantify the dominant water transport mode, and (ii) to attribute a self-humidification quality to the produced electric power, innovatively identifying which transport mode prevails and *how* a given power density is produced in terms of external water need, thus proposing a new method to design highly-efficient and self-humidified PEM fuel cells.

1. Introduction

The urgency to decarbonize the power generation process has recently grown to an unprecedented priority in several sectors [1]. These are approximately divided among hard-to-decarbonize ones, where viable alternatives to combustion-based processes are not a short-term achievement, and others where mature technologies already exist to mitigate their carbon footprint. The transportation sector encompasses both classes due to its wide diversity, with mobility areas still based on high energy density liquid fuels (e.g., aviation, shipping, etc.) relying on carbon-neutral synthetic fuels for their decarbonization (e.g., e-fuels or sustainable aviation fuels, [2]), alongside others where the direct electrification already permits zero local emissions (e.g. light-duty transportation). In this context, one of the strategies to design an electric vehicle is to use fuel cells for electricity generation from on-board stored hydrogen, leveraging the higher energy density of hydrogen storage than that of batteries [3,4] and the power density progress made in the last decades for PEMFC. This type of electric vehicles (FCEVs, Fuel Cell Electric Vehicles) well complements the on-board energy limitation of Battery Electric Vehicles (BEVs), representing a hydrogen-based

technology to extend the decarbonization of transportation [5]. Two development routes have been pursued to lower the specific cost of PEMFCs (i.e., cost per unit of generated power), namely the use of ultra-thin membranes and the reduction of externally supplied humidity, with the former aiming at increasing the specific power and efficiency and the latter addressed to a system complexity and cost reduction. However, both directions are tightly interconnected, and their joint analysis is the core of this study.

The use of thin membranes extremizes the "zero-gap" concept of electrode distance minimization. Their advantage in reducing the ohmic losses are a well-known effect, as measured by Tabuchi et al. [6] comparing 30 μm and 6 μm Nafion membranes on a laboratory-scale low-temperature PEMFC, and a product-level confirmation of such concept lies in the 10 μm Nafion membrane of the Toyota Mirai fuel cell powertrain [7]. However, the reduced separator thickness amplifies the gas crossover, due to the reduced diffusion distance between anodic/cathodic gas mixtures where concentration gradients increase. Therefore, a Fickian-type diffusion flux originates on the entire membrane and electrode assembly (MEA) area. The consequences of gas crossover are multiple, and they span from the waste of reactants, the onset of degradation mechanisms, the need of frequent purges, and the

^{*} Corresponding author at: Dipartimento di Ingegneria "Enzo Ferrari", Università degli Studi di Modena e Reggio Emilia, Via P. Vivarelli 10 41125 Modena, Italy.
E-mail address: alessandro.dadamo@unimore.it (A. d'Adamo).

Nomenclature	
<i>List of Abbreviations</i>	
ABP	Anodic Bipolar Plate
ACL	Anodic Catalyst Layer
AGDL	Anodic Gas Diffusion Layer
BEV	Battery Electric Vehicle
BP	Bipolar Plate
CBP	Cathodic Bipolar Plate
CCL	Cathodic Catalyst Layer
CGDL	Cathodic Gas Diffusion Layer
CFD	Computational Fluid Dynamics
CL	Catalyst Layer
EOD	Electro-Osmotic Drag
ePTFE	Expanded polytetrafluoroethylene
FCEV	Fuel Cell Electric Vehicle
FoM	Figure Of Merit
FV	Finite Volume
GDL	Gas Diffusion Layer
HHV	Higher Heating Value
LE	Liquid-equilibrated
MEA	Membrane and Electrode Assembly
MMP	Mixture Multi-Phase
PEM	Polymeric Electrolyte Membrane
PEMFC	Polymeric Electrolyte Membrane Fuel Cell
PFSA	Perfluorosulfonic acid
RD	Retro-Diffusion
RH	Relative Humidity
VE	Vapour-equilibrated
<i>List of Symbols</i>	
α_l	Liquid volume fraction [-]
c	Molar concentration [mol m^{-3}]
c_p	Specific heat [$\text{J kg}^{-1} \text{K}^{-1}$]
$\Gamma_{EOD/RD}$	MEA dominant transport index [-]
Γ_{p^*}	Self-humidification index of the power density [-]
$D_{k,0}$	Diffusivity coefficient of the k -th species at standard conditions [$\text{m}^2 \text{s}^{-1}$]
D_k^{eff}	Effective diffusivity coefficient of the k -th species [$\text{m}^2 \text{s}^{-1}$]
δ_0	Nominal membrane thickness [μm]
δ_{eff}	Effective membrane thickness [μm]
ϵ	Porosity [-]
η	Overpotential [V]
F	Faraday's constant [C mol^{-1}]
i	Current density [A cm^{-2}]
$i_{0, a/c}$	Anodic/cathodic exchange current density [A cm^{-2}]
i_e	Ionic current density [A cm^{-2}]
i_s	Electronic current density [A cm^{-2}]
$\lambda_{a/c}$	Anodic/cathodic stoichiometric ratio [-]
λ	Membrane water content [-]
h_{lat}	Mass-specific latent heat [$\text{m}^2 \text{s}^{-2}$]
k_C / k_E	Condensation and evaporation rate constant [s^{-1}] / [$\text{Pa}^{-1} \text{s}^{-1}$]
k^{eff}	Effective thermal conductivity coefficient [$\text{W m}^{-1} \text{K}^{-1}$]
K_i	Membrane permeability for the i th species [$\text{mol m}^{-1} \text{s}^{-1} \text{Pa}^{-1}$]
\dot{m}_{ec}	Mass transfer rate for phase transition [kg s^{-1}]
\dot{m}_{EOD}	Water mass flux due to electro-osmotic drag [$\text{kg m}^{-2} \text{s}^{-1}$]
\dot{m}_{RD}	Water mass flux due to retro-diffusion [$\text{kg m}^{-2} \text{s}^{-1}$]
M_k	Molecular weight of the k -th species [kg mol^{-1}]
n_d	Electro-osmotic drag coefficient [-]
P''	Power density [W m^{-2}]
ρ_m	Mixture density [kg m^{-3}]
σ_e	Ionic conductivity [S m^{-1}]
σ_s	Electronic conductivity [S m^{-1}]
S_{cap}	Momentum source term due to capillary transport in porous media [$\text{kg m}^{-2} \text{s}^{-2}$]
S_h	Energy source term due to phase transition [$\text{kg m}^{-1} \text{s}^{-3}$]
S_i	Membrane solubility for the i th species [$\text{mol m}^{-3} \text{Pa}^{-1}$]
S_j	Proton/water source term in the Nernst-Planck equation [$\text{mol m}^{-2} \text{s}^{-1}$]
S_k	Mass fraction source term for the k -th species [-]
S_m	Mass source term for mass [$\text{kg m}^{-3} \text{s}^{-1}$]
$S_{ph, tr}$	Phase-transition heat source term [$\text{kg m}^{-1} \text{s}^{-3}$]
S_{Φ_e}	Ionic potential source term [A m^{-3}]
S_{Φ_s}	Electronic potential source term [A m^{-3}]
S_T	Source term for energy equation [$\text{kg m}^{-1} \text{s}^{-3}$]
S_V	Momentum source term due to porous fluidic resistance [$\text{kg m}^{-2} \text{s}^{-2}$]
ϑ	Contact angle of porous media surfaces [deg]
x_w^g	Water vapour molar fraction [-]
$x_{w, sat}$	Water molar fraction at saturation [-]
Y_k	Mass fraction of the k -th species [-]
V_m	Mixture velocity [m s^{-1}]
V_{mem}	Partial molar volumes of the dry membrane [$\text{m}^3 \text{mol}^{-1}$]
V_0	Partial molar volumes of water [$\text{m}^3 \text{mol}^{-1}$]
z_k	Number of exchanged charges for the k -th species reaction [-]

reduction of the cell potential. Regarding the waste of reactants, a utilization decrease of both hydrogen and oxygen is created by their membrane crossover, as a portion of molecules does not participate to electrochemical reactions, as well as inducing degradation mechanisms [8]. Focusing on nitrogen, its crossover to the anode is detrimental in closed-loop anodic layouts, where the excess hydrogen is recirculated to maximize its utilization, leading to the accumulation of nitrogen traces requiring frequent anodic purges, ultimately increasing the fuel waste [9]. Finally, the non-used electronic charges associated to leaked reactants lower the cathodic cell potential and increase the anodic one, globally reducing the useful cell voltage (crossover overpotential, η_x). All these aspects are inversely proportional to the membrane thickness; hence a detrimental impact is to be expected for ultra-thin membranes, which has to be weighed against the beneficial reduction in internal cell's resistance.

Regarding the techniques to obtain self-humidifying MEAs, these have been long researched in view of the potential to eliminate the

humidifiers from fuel cell systems, leveraging the internal water diffusion permitted by ultra-thin membranes. Jung et al. [10] proposed a thin-film dual-layered electrode concept able to provide equal performance under dry conditions than conventional electrodes under fully humidification. Ultra-thin (5 μm thickness) membranes were realized and tested by Kienitz et al. [11], and the expected performance gain over thicker counterparts was confirmed in view of their reduced ohmic losses. Moreover, the ePTFE (expanded polytetrafluoroethylene) reinforcement granted sufficient resistance to degradation to satisfy the Department of Energy (DOE) targets [12], and the reduced membrane thickness was postulated to contribute to a better self-humidification by mitigating the anode de-hydration, although this was not quantified, thus projecting this technology to an effective market application. The consequence of thin membranes use on vehicle range was analytically modelled by Kienitz [9], where a simple model was proposed to weight the benefits of higher cell efficiency with the lower hydrogen utilization due to more frequent anodic purges. The study numerically identified

the membrane thickness optimizing both aspects, hence maximizing the expected vehicle range, and reinforcing it as a key cell design parameter. However, the presented study used a simplified PEMFC model, without discussing the effect of different flow rates and assuming a linear ohmic resistance variation with its thickness (hence constant conductivity), which implies an assumedly identical water management under all conditions.

However, in the authors' opinion a knowledge gap still exists in comprehensively consider the electric and water balance of ultra-thin membranes, and to objectively measure the degree of self-humidification of a PEMFC, which is still based on qualitative considerations. To achieve this research target, in this paper a model for the polymeric membrane of PEMFCs is implemented in a commercial 3D-CFD software, including the water-related processes (phase transition, electro-osmotic drag, liquid water back-diffusion) and the effect of gas crossover (H₂, O₂, N₂, H₂O) on mass transport and cell potential. The analysis starts from a model validation on the results of a test hydrogen-air PEMFC using two membrane thicknesses (30 μm and 6 μm) under high flow rate conditions [6], as typical from laboratory-scale studies. Then, the same analysis is numerically extended to a low stoichiometry operation ($\lambda_{a/c} = 2.0$), more relevant for the practical use of PEMFCs, and the electric performance and self-humidification degree are discussed for the different flow rates and membrane thicknesses. Two original figures of merit are proposed to (i) quantify the dominant water transport mode between electro-osmotic drag and back-diffusion, associated to the external water supply, and (ii) to attribute a self-humidification index to the produced electric power density. The simulation results reinforce the design direction of minimization of the membrane thickness to reduce the cell's resistance for a high efficiency and to operate under low flow rates to further promote the MEA's self-humidification. The quantification of the gaseous crossover fluxes is also provided to include the mass transport of hydrogen, oxygen, nitrogen and water vapour, hence presenting a comprehensive analysis to understand the effects of ultra-thin membranes in PEMFCs.

2. Methodology

2.1. Governing Equations for fluid and solid parts

In this study the governing equations for the multi-dimensional, non-isothermal and multi-phase simulation of transport processes in PEMFCs are adopted. This approach is detailed in [13–15] and will be resumed in the following. It consists of a unified set of coherent governing equations applicable to all cell domains (fluid, porous, solids), hence inherently granting flux continuity at interfaces, and applying the assumptions of steady-state and laminar flow.

In the limits of the Mixture Multi-Phase (MMP) approach, the mass (continuity) and momentum conservation are expressed as in Eq. (1) and 2, with ε being the porosity of the porous media, ρ_m and \mathbf{V}_m the mixture density and velocity, and S_m the apparent mass creation/destruction at Catalyst Layers (CLs) due to electrochemical reactions. Regarding the mixture momentum conservation, in addition to the pressure gradient (∇p) and the viscous resistance expressed by the molecular viscosity (μ), the source terms given by the fluidic resistance opposed by porous materials (S_v) and by capillary effects (S_{cap}) are included. The former is modelled using a Darcy's law model based on the porous material permeability (K) as in Eq. (3), whereas the latter is modelled using an empirical Leverett [16] function based on the liquid volume fraction (α_l), as in Eq. (4). They are applied both to Gas Diffusion Layers (GDLs) and CLs, with specific properties in each part.

$$\nabla \cdot (\varepsilon \rho_m \mathbf{V}_m) = S_m \quad (1)$$

$$\nabla \cdot (\rho_m \varepsilon^2 \mathbf{V}_m \mathbf{V}_m) = -\nabla p + \nabla \cdot (\mu \varepsilon \nabla \cdot \mathbf{V}_m) + S_v + S_{cap} \quad (2)$$

$$S_v = -\frac{\mu}{K} \varepsilon \mathbf{V}_m \quad (3)$$

$$S_{cap} = \sigma \cdot \cos \theta \cdot \left(\frac{\varepsilon}{K}\right)^{0.5} \cdot \nabla J(\alpha_l) \quad (4)$$

The scalar species transport is modelled as in Eq. (5) for H₂, O₂, N₂ and H₂O in terms of mass fractions of the generic k -th constituent (Y_k). An effective diffusivity coefficient in porous media (D_k^{eff}) is calculated as a function of a reference value at standard conditions ($D_{k,0}$), which is modified based on temperature, pressure, and applying a Bruggemann's correction to account for porosity effect (Eq. (6)). The k -th volumetric species source term (S_k) is calculated by the Faraday's law (Eq. (7)), expressing the linear proportionality between reactants/product conversion rate into/from electric volumetric current density (j) at CLs, with z_k being the number of transferred charges, F the Faraday's constant, and M_k the molecular weight.

$$\nabla \cdot (\rho_m Y_k \varepsilon \mathbf{V}_m) = \nabla \cdot (\rho_m D_k^{eff} \nabla Y_k) + S_k \quad (5)$$

$$D_k^{eff} = \left[D_{k,0} \cdot \left(\frac{T}{T_0}\right)^{1.5} \cdot \left(\frac{p_0}{p}\right) \right] \cdot \varepsilon^{1.5} \quad (6)$$

$$S_k = \pm \frac{j}{z_k F} M_k \quad (7)$$

The energy conservation is expressed by Eq. (8) as a function of specific heat (c_p), an effective thermal conductivity coefficient (k^{eff}) and an energy source term (S_T). This reproduces all the local heat source/sink effects (Eq. (9)), i.e. the Joule effect at electronic and ionic conducting parts (with i_s and i_e being their respective superficial current density, and σ_s and σ_e their respective charge conductivity coefficients), the activation overpotential (η_{act}), the molar entropy variation ($\Delta \bar{s}$) and the heat transfer due to phase transition ($S_{ph.tr}$). The charge conservation follows a diffusive-type differential equation (Eqs. (10) and 11) for the electronic and ionic charge transport, with electric potential sources as driving forces (Φ_s and Φ_e , respectively).

$$\nabla \cdot [(\rho_m c_p)^{eff} T \mathbf{V}_m] = \nabla \cdot (k^{eff} \nabla T) + S_T \quad (8)$$

$$S_T = \left(\frac{i_s^2}{\sigma_s^{eff}} + \frac{i_e^2}{\sigma_e^{eff}} \right) + j \eta_{act} + j \frac{T \cdot \Delta \bar{s}}{z_k F} + S_{ph.tr} \quad (9)$$

$$\nabla \cdot (\sigma_s^{eff} \nabla \Phi_s) + S_{\Phi_s} = 0 \quad (10)$$

$$\nabla \cdot (\sigma_e^{eff} \nabla \Phi_e) + S_{\Phi_e} = 0 \quad (11)$$

2.2. Modelling of water phase transition

The water phase change is modelled implementing the Sangtabi et al. [17] formulation for inter-phase mass transfer rate due to evaporation/condensation (\dot{m}_{ec} , [kg s⁻¹]) reported in Eq. (12), where k_C [s⁻¹] and k_E [Pa⁻¹ s⁻¹] are condensation and evaporation rate constants, α_l is the volume fraction of liquid, x_w^g refers to the corresponding mole fraction in gaseous state and $x_{w,sat}$ at saturation, ρ_l is the density of the liquid phase and M_w is the water molar weight.

$$\dot{m}_{ec} = \begin{cases} k_C (1 - \alpha_l) \frac{M_w}{R T} p (x_w^g - x_{w,sat}) & \text{if } x_w^g \geq x_{w,sat} \\ k_E \alpha_l \rho_l p (x_w^g - x_{w,sat}) & \text{if } x_w^g < x_{w,sat} \end{cases} \quad (12)$$

The local \dot{m}_{ec} is introduced as a mass source term for the gaseous and liquid water, alongside a volumetric heat source (S_h , [kg m⁻¹ s⁻³]) related to the latent heat of phase transition (h_{lat} [m² s⁻²]), as in Eq. (13):

$$S_h = \dot{m}_{ec} h_{lat} \quad (13)$$

2.3. Governing Equation for polymeric membrane

The modelling of the protons and liquid water transport across the solid PEM is based on the Nernst-Planck equation [14], which uses a concentrated solution approach to calculate the molar flux (J_j) of the diluted j -th species (Eq. (14)) as composed by the contributions of a migration, diffusive, convective, and source terms (right-hand side of Eq. (14)) in the solvent. In a solid electrolyte as that of PEM, the solvent convective term is always null ($\mathbf{V}_{solv} = 0$).

$$\mathbf{J}_j = -z_j \theta_j F c_j \nabla \Phi_j - D_j \nabla c_j + c_j \mathbf{V}_{solv} + \mathbf{S}_j \quad (14)$$

When Eq. (14) is applied to protons transport, the assumption of a uniform H^+ concentration across the reduced membrane thickness is made ($\nabla c_j = 0$), with the molar flux depending on the proton mobility, related to the proton diffusivity via the Nernst-Einstein equation stating $D_j = R T \theta_j$, and driven by the ionic potential gradient ($\nabla \Phi_j$), without source terms as in the solid polymer no redox reactions occur. The same equation can be applied to calculate the molar flux of the dissolved water, where the assumption of charge-neutral species ($\nabla \Phi_j = 0$) leads to a diffusion-driven flux. The source term here is used to introduce the electro-osmotic drag effect (Eq. (15)), which is peculiar of the perfluorosulfonic acid (PFSA) acid membranes, and which expresses the dissolved water transport operated by the ionic current.

$$\mathbf{S}_j = \frac{n_d \mathbf{i}_e}{F} \quad (15)$$

The electro-osmotic drag coefficient (n_d) quantifies the statistical number of water moles dragged per proton mole, and in this study it is expressed as in Eq. (16) [18] as linearly proportional to the membrane water content (λ). This is related to the dissolved water concentration (c_w) and to the membrane dry density and equivalent weight ($\rho_{m,dry}$ and EW , respectively), as in Eq. (17). The membrane water content is calculated from the local water activity, here assumed equivalent to the relative humidity (RH) of the adjacent CLs, as in Eq. (18) [18]:

$$n_d = \frac{2.5}{22} \lambda \quad (16)$$

$$\lambda = \frac{EW}{\rho_{m,dry}} c_w \quad (17)$$

$$\lambda = 0.043 + 17.81 \cdot RH - 39.85 \cdot RH^2 + 36.0 \cdot RH^3 \quad (18)$$

While Eq. (18) allows to infer the membrane water content from the adjacent reagents' humidity, hence providing a closure to Eq. (14) for the dissolved water transport, it also affects the membrane ionic conductivity via Eq. (19) [18], with influence also on heat generation (Eq. (9)) and ionic current conservation (Eq. (11)).

$$\sigma_e = (0.5139 \lambda - 0.326) \cdot e^{1268 \left(\frac{1}{303} - \frac{1}{T} \right)} \quad (19)$$

This set of equations embodies the two-way coupling between ionic current and dissolved water transport, and it underlines the relevance of an accurate modelling of both aspects for the interconnected hydric-electric description of the MEA processes.

The described approach is based on the concept of the polymeric membrane as a macro-homogeneous continuum, simplifying its fundamental structure of a hydrophobic polymeric chain with negatively charged hydrophilic sulfonic acid groups (SO_3^-). This mixed hydrophobic/hydrophilic behaviour is at the basis of the unrivalled ionic conductivity of PFSA acid electrolytes, although it requires a careful water balance for optimal cell operation. This picture is further complicated by the possible membrane contact with multi-phase vapour/liquid water reservoirs at CL interfaces, as described by the Weber et al. [19–21] model and referred to as “vapour-“ and “liquid-equilibrated” conditions (VE and LE, respectively). These extreme are used to explain the

Schroeder's paradox, i.e., a discontinuity in membrane water content from $\lambda \simeq 14$ (VE) to $\lambda \simeq 22$ (LE) under an equal water activity. In [19, 20] this is motivated by the membrane structural change, evolving from the pore-like membrane structure ($\lambda \simeq 14$, where the water-filled ionic pores do not form pathways to increase the water uptake, similarly to a collapsed channels network), to a liquid-filled channel concept ($\lambda \simeq 22$). These conditions are believed to be both present under fully saturated conditions, acting in parallel.

The membrane swelling due to water uptake is another aspect considered in this model, as the through-plane thickening of a fully-hydrated membrane increases the conductive path (δ_{eff}) for protons, dissolved water, and gas crossover, with respect to the nominal distance (δ_0). This is represented by Eq. (20) [20], where $V_w = M_w/\rho_w$ and $V_m = EW/\rho_m$ are the molar volumes of water and of the dry ionomer, respectively.

$$\frac{\delta_{eff}}{\delta_0} = 1 + 0.36 \frac{\lambda V_w}{V_m} \quad (20)$$

Considering the modelling convenience in neglecting the effects of the swelling on the finite volume (FV) discretization of the MEA and of the adjacent parts, the effect on local transport is accounted for by means of an effective ionic conductivity ($\sigma_{e,eff}$, Eq. (21)), whereas all the species transport modes (dissolved water and gas crossover) will consider the effective distance δ_{eff} .

$$\sigma_{e,eff} = \sigma_e \left(\frac{\delta_{eff}}{\delta_0} \right)^{-1} \quad (21)$$

2.4. Modelling of gas crossover

Gas crossover results from the imperfect fluidic separation of the polymeric membrane. It is an undesired phenomenon as it (i) lowers the cell potential due to the anodic/cathodic crossover overpotentials ($\eta_{x,a/c}$), (ii) leads to reactants leakage to counter-electrodes, (iii) induces secondary processes precursors for membrane degradation (e.g., H_2O_2 formation at anode [8], etc.), and (iv) pollutes the anodic flow with leaked nitrogen, leading to fuel-wasting periodic purging of the anodic compartment.

The nature of gas crossover through the electrolyte is essentially a diffusive-type transport, where the membrane is assumed as a porous medium and a species molar flux is driven by concentration and/or pressure gradients. The present study focuses on concentration gradients, which are always present due to the different anodic and cathode flow composition, and whose modelling follows a diffusive (Fickian) rather than hydraulic model. Moreover, anodic/cathodic pressures are equal in this study, hence the pressure differential is absent. The diffusive model is based on the molar concentration gradient of the generic i -th species in the CL portion adjacent to the membrane surface (∇c_i), and based on a diffusivity coefficient (D_i , [$m^2 s^{-1}$]) and the thickened membrane distance (δ_{eff}), the molar flux (J_i , [$mol m^{-2} s^{-1}$]) can be expressed as in Eq. (22). This equation is also used to model the diffusive transport of liquid water (“retro-diffusion”), as it shares the same fundamental nature.

$$\mathbf{J}_i = -D_i \nabla c_i \quad (22)$$

However, the diffusivity coefficient is related to permeability (K_i , [$mol m^{-1} s^{-1} Pa^{-1}$]) by means of the species solubility (S_i , [$mol m^{-3} Pa^{-1}$]), as in Eq. (23). The substitution of Eq. (23) into Eq. (22) leads to Eq. (24), where J_i is expressed a function of the partial pressure gradient (∇p_i) and of the membrane thickness.

$$K_i = S_i D_i \quad (23)$$

$$\mathbf{J}_i = -K_i \nabla p_i \quad (24)$$

Eq. (22) and 24 can be indifferently used to model the species crossover rate, allowing to flexibly use experimental data both in the

form of D_i or K_i measurements. Species crossover fluxes are implemented in the 3D-CFD model via local user-defined source mass terms for each species at anodic and cathodic catalyst layer (ACL and CCL, respectively), where concentration and pressure gradients across the membrane are spatially resolved via the local (cell)-based calculation, and mass conservation is granted by the opposite sign of anodic/cathodic terms for a given species. Expressions for the hydrogen diffusivity or permeability through Nafion were proposed by Bernardi et al. [22], Kocka et al. [23], Weber et al. [20], Cheng et al. [24], and by Schoemaker et al. [25], while nitrogen values are reported in Baik et al. [26] and in [23], oxygen values by Mench [27] and Weber et al. [20], and water vapour values by Springer et al. [18] and Motupally et al. [28].

In this study Eq. (25) from [20,29] and Eq. (26) from [20] are used for the permeability coefficients of H_2 and O_2 , respectively, with V_{mem} and V_0 being partial molar volumes of the dry membrane and of water, respectively. For N_2 permeability, the constant value from [23] is used ($K_{N_2} = 1.5 \times 10^{-14} \text{ mol m}^{-1} \text{ s}^{-1} \text{ Pa}^{-1}$) while for water diffusivity Eq. (27) from [18] is used.

$$K_{H_2} = \left(2.2 \times 10^{-11} \frac{\lambda V_0}{V_{mem} + \lambda V_0} + 2.9 \times 10^{-12} \right) e^{\left[\frac{21000}{R} \left(\frac{1}{T_{ref}} - \frac{1}{T} \right) \right]} \times 10^{-3} \quad (25)$$

$$K_{O_2} = \left(1.9 \times 10^{-11} \frac{\lambda V_0}{V_{mem} + \lambda V_0} + 1.1 \times 10^{-12} \right) e^{\left[\frac{22000}{R} \left(\frac{1}{T_{ref}} - \frac{1}{T} \right) \right]} \times 10^{-3} \quad (26)$$

$$D_w = e^{\left[\frac{2416}{303} \left(\frac{1}{303} - \frac{1}{T} \right) \right]} (2.563 - 0.33 \lambda + 0.0264 \lambda^2 - 0.000671 \lambda^3) \times 10^{-10} \quad (27)$$

The effect of oxygen and hydrogen leakage also affects the crossover overpotential, as the loss of reactants molecules reduces the chemical potential for the electrochemical reaction. This effect is modelled based on the species crossover flux as in Eq. (22) or 24, which is converted into an equivalent current density using the Faraday's law. Finally, this leads to a crossover overpotential at anode/cathode ($\eta_{x,a/c}$) using a Tafel approach (Eq. (28)), where the electrode exchange current density ($i_0, a/c$) is used.

$$\eta_{x,a/c} = \frac{R T}{\alpha F} \ln \left(\frac{z F |J_i|}{i_0, a/c} \right) \quad (28)$$

Considering the higher anodic exchange current density than the hydrogen crossover current density, the impact of the hydrogen crossover flux on the anodic overpotential is negligible and the Tafel approximation cannot be applied, therefore the anodic crossover overpotential is neglected. Conversely, at cathode the oxygen crossover flux is higher than the cathodic exchange current density, allowing the use of Eq. (28). The modelling of crossover overpotential is important when ultra-thin membranes are of interest, due to its potentially large effect in lowering the useful cell voltage.

3. Numerical model

The numerical domain reproduces the geometry of the test cell used in [6], i.e. a 10 mm long channel with a square-section channel (1.0 mm side). The bipolar plate rib separating the channels is 1 mm wide, hence creating a uniformly spaced channel-rib design with 1.0 mm pitch. In [6] several configurations were tested in a co-flow arrangement, among which the comparison of the mentioned design with narrow channel-rib ones (as low as 0.1 mm pitch) for the same 30 μm -thick membrane, and the comparison of the 1.0/0.4 mm pitch cases was simulated and discussed in [30,31]. In this study, a different analysis is carried out, focusing on the effect of the membrane thickness variation in the 1.0 mm

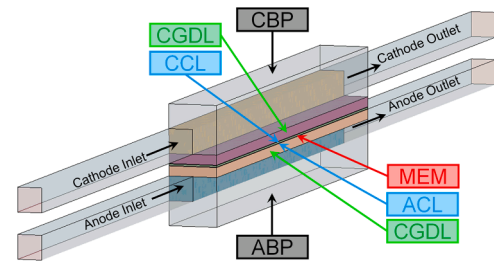


Fig. 1. Simulated domain with labelled anodic/cathodic bipolar plates (ABP, CBP), gas diffusion layers (AGDL, CGDL), catalyst layers (ACL, CCL) and membrane (MEM), with indication of the co-flow arrangement and channel extrusions in transparency.

Table 1

Main material properties used in CFD models.

Component / Sub-model	Property	Value	Unit
GDL	Porosity	0.7	-
	Permeability	5.7×10^{-12}	m^2
	Contact angle	10^{-12}	deg
CL	Porosity	110	-
	Permeability	0.4	-
	Contact angle θ_c	2.6×10^{-13}	deg
	i_{ion}	110°	kg/m^3
	Density	2000	S/m
	Ion. ConductivityIon.	Eq. (19)	$\text{J kg}^{-1} \text{K}^{-1}$
	Spec. HeatIon.	903	$\text{W m}^{-1} \text{K}^{-1}$
	Th. ConductivityIon.	0.445	-
	Volume Fraction	0.6	kg/m^3
	Pt/C	2250	S/m
	DensityPt/C	500	$\text{J kg}^{-1} \text{K}^{-1}$
BP	El. ConductivityPt/C	707.68	kg m^{-2}
	Spec. HeatPt/C	10	-
	Th. Conductivity	0.004	-
	m_{Pt}	0.4	-
	Volume Fraction	2250	kg m^{-3}
	Density	20,000	S m^{-1}
	El. Conductivity	707.68	$\text{J kg}^{-1} \text{K}^{-1}$
Membrane	Spec. Heat	20	$\text{W m}^{-1} \text{K}^{-1}$
	Th. Conductivity	2000	kg m^{-3}
	Density	Eq. (19)	S m^{-1}
	Ion. Conductivity	903	$\text{J kg}^{-1} \text{K}^{-1}$
Contact Resistances	Spec. Heat	0.445	$\text{W m}^{-1} \text{K}^{-1}$
	Th. Conductivity	2×10^{-8}	$\text{m}^2 \Omega$
	Electrical contact resistance	3×10^{-4}	$\text{m}^2 \text{K W}^{-1}$
	Thermal contact resistance	Eq. (25)	$\text{mol Pa}^{-1} \text{m}^{-1} \text{s}^{-1}$
Species crossover flux	H_2 permeability coefficient	Eq. (25)	$\text{mol Pa}^{-1} \text{m}^{-1} \text{s}^{-1}$
	O_2 permeability coefficient	Eq. (26)	$\text{mol Pa}^{-1} \text{m}^{-1} \text{s}^{-1}$
	N_2 permeability coefficient	Eq. (26)	$\text{mol Pa}^{-1} \text{m}^{-1} \text{s}^{-1}$
	H_2O vapour diffusivity coefficient	Eq. (27)	$\text{mol Pa}^{-1} \text{m}^{-1} \text{s}^{-1}$

pitch design. The membrane was reduced in [6] from 30 μm to a 6 μm thickness, using the same CL (10 μm thick), GDL (200 μm thick), and channel/bipolar plate configuration. Fig. 1 represents the simulated domain, highlighting that the cell is specular with respect to the MEA plane, with identical anodic and cathodic parts, and that an axial symmetry plane is used to simulate half of the domain.

Catalyst layers are modelled with a macro-homogeneous approach based on a porous media model for fluids (reactants and products), with a bi-component solid phase able to transport protons (ionomeric phase) and electrons (Pt/C support), and where electrochemical surface reactions are modelled using a Butler-Volmer formalism. This model has been validated in [31] and used for PEMFC modelling studies in [32–34]. Porous media permeability is evaluated as a function of the

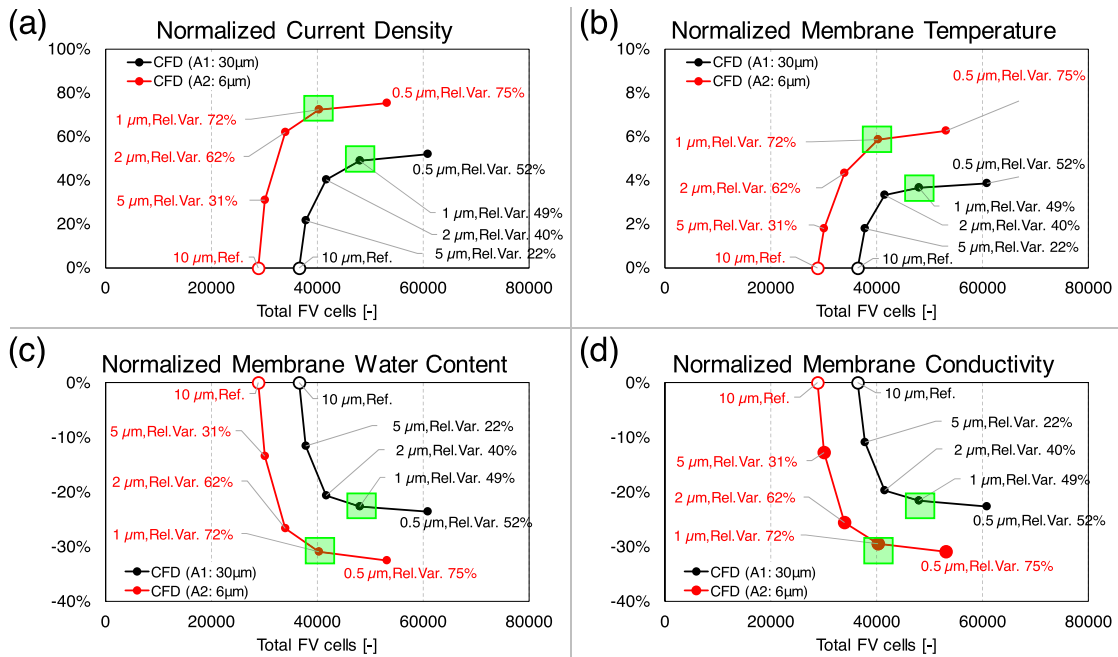


Fig. 2. Mesh sensitivity analysis on the CL resolution at 0.4 V considering (a) current density, (b) membrane temperature, (c) membrane water content, and (d) membrane ionic conductivity, with values normalized on the 10 μm resolution case (1 layer), for both A1 (black, 30 μm membrane thickness) and A2 (red, 6 μm membrane thickness) cases at 0.4 V. The CL resolution selected for the model creation is green boxed.

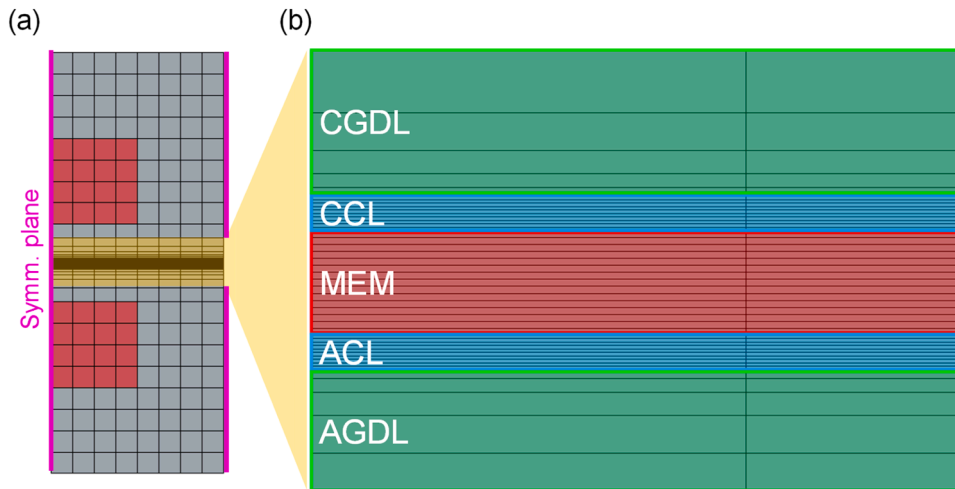


Fig. 3. Through-plane section of (a) the FV grid for the 30 μm membrane case, with (b) close-up to highlight the on the membrane (2 μm resolution), CLs (1 μm resolution) and part of the GDLs.

specific porosity as indicated in [35], with calculated values reported in Table 1.

A structured hexahedral FV mesh is used, with a uniform grid resolution (2 μm) in the through-plane direction which is used for all cases, resulting in 15 and 3 cell layers for the 30 μm and the 6 μm membrane models, respectively. Among the other components, the choice of the CL resolution is critical for the adopted modelling framework, not only due to the expected high through-plane gradients, but also because several membrane parameters, source terms, and species fluxes will involve variables calculated at CLs. The mesh sensitivity study to the CL resolution is reported in Fig. 2. A dedicated mesh sensitivity analysis is carried out increasing the through-plane resolution of the FV grid at CLs from 10 μm (1 layer) to 0.5 μm (20 layers). The variation of current density, membrane temperature, water content, and ionic conductivity at 0.4 V for progressively higher resolution cases are observed with

respect to a 10 μm case (coarsest resolution, 1 cell layer for the entire CL), which is assumed as the reference case. This is carried out for the 30 μm and the 6 μm membrane thicknesses (named A1 and A2, respectively), a relative invariance of all quantities is observed increasing the grid resolution from 1 μm to 0.5 μm. Considering the relevant increase in the total FV cells for higher resolutions, and the invariance in the electrical/thermal results, the 1 μm resolution (10 layers) is chosen for CLs.

A progressive grid resolution reduction in the GDLs is created moving from the MEA to the channel and bipolar plate regions to lower the computational cost, as visible in Fig. 3. As for the in-plane directions (parallel and normal to the channel axis) a uniform grid resolution of 0.125 mm is adopted, and 10-mm extrusions are added at both inlet and outlets for numerical stability. Symmetry planes are used to reduce the computational cost, allowing the simulation of half channel-rib assembly while applying a no-normal flux (symmetry) condition at both sides

Table 2
List of simulated cases.

	High Stoichiometry	Low Stoichiometry
Thick Membrane (30 μm)	Case Label: A1 Mem. Thickness: 30 μm Reactants Stoich.: high [6].	Case Label: B1 Mem. Thickness: 30 μm Reactants Stoich.: low ($\lambda_{a/c} = 2.0$).
Thin Membrane (6 μm)	Case Label: A2 Mem. Thickness: 6 μm Reactants Stoich.: high [6].	Case Label: B2 Mem. Thickness: 6 μm Reactants Stoich.: low ($\lambda_{a/c} = 2.0$).

of the domain. The total number of FV cells is 48,000 and 40,320 for the 30 μm and the 6 μm membrane models, respectively. In Table 1 the main material properties used in the model are reported. The operating conditions used in the cell validation in [6] were that of a high anodic and cathodic flow rate (2.0 L/min), with 90 % relative humidity at 80 °C at inlets, and 2.5 bar as operating pressure. The cathodic crossover overpotentials are calculated as 0.024 / 0.048 V for the 30 / 6 μm membrane thickness cases, respectively.

In the first part of the study, the same operating conditions reported in [6] are used for model validation. However, the high flow rate that is typically used in validation studies, e.g. in the “zero-gradient” test conditions reported in [36], corresponds to elevated stoichiometric ratios at anode and cathode ($\lambda_{a/c}$), defined as the ratio between the anodic/cathodic inlet flow rate over the electrochemical reaction rate of hydrogen or oxygen, respectively. The operation at high $\lambda_{a/c}$ is far from the conditions of practical interest, where the delicate balance of the cathodic air flow rate dictated by the power request of the air compressor compels to operate at much lower stoichiometric ratios. Hence, in the second part the analysis moves to anodic/cathodic stoichiometric factors of 2.0 ($\lambda_{a/c} = 2.0$), which is deemed as a realistic operating value. Simulation

results will be used to investigate how this affects the water balance, the entity of gas crossover, and the overpotentials, to obtain a comprehensive view of both the effect of thin membrane use and that of low flow rates. For the sake of conciseness, the investigated cases are hereafter named as in Table 2.

4. Results

4.1. Results and validation at high stoichiometry

The simulated polarization and power density curves for the 30 μm and the 6 μm cases operated at the test conditions (high reactants flow rates, Cases A1-A2) are reported in Fig. 4a-b, spanning a voltage range from 0.4 to 1.0 V with a 0.1 V resolution. The different current-voltage relationship is in agreement with the experimental data from [6], although a small current density overestimation is predicted for the lowest voltage (0.4 V), with the thin membrane case (A2) showing lower ohmic losses than the thick membrane one (A1) thanks to the shorter conductive distance between the electrodes for a globally lower cell resistance. The simulation results confirm the robustness of the numerical framework not only under different electric potentials and currents, but also for largely different membrane thicknesses.

However, a deeper investigation of the differences between A1 and A2 cases reveals the full scale of processes influenced by the membrane thickness, each contributing to the cell’s electric resistance and water balance. The average RH at ACL/CCL is reported in Fig. 5, showing that while at CCL a stable RH value is observed due to protons-dragged water (electro-osmotic drag effect, EOD) adding to the electrochemically produced water, at the ACL a severe de-hydration occurs. The membrane drying worsens under high current operation, as illustrated by the spatial distribution of RH is reported in Fig. 6 at ACL/CCL for the 0.4 V cases. These are selected as those with the highest current density for

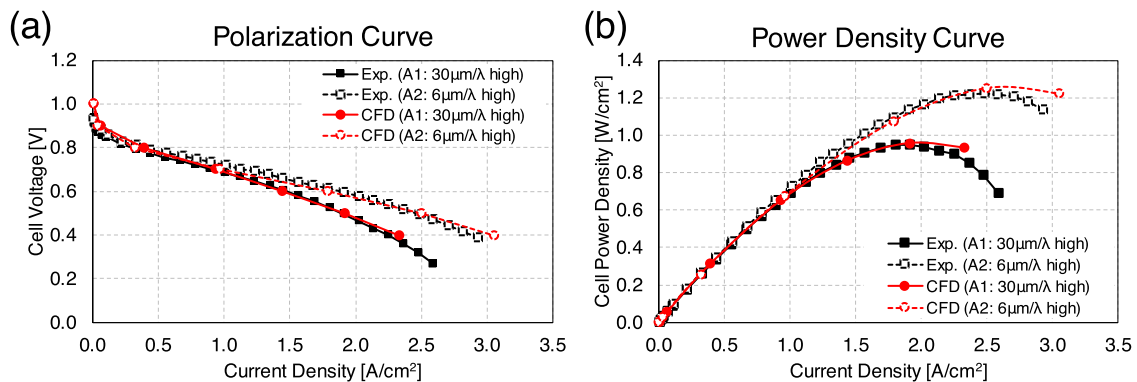


Fig. 4. (a) Polarization curves and (b) power density curves for the A1 and A2 cells at test conditions: experiments from [6] (black), and CFD results (red).

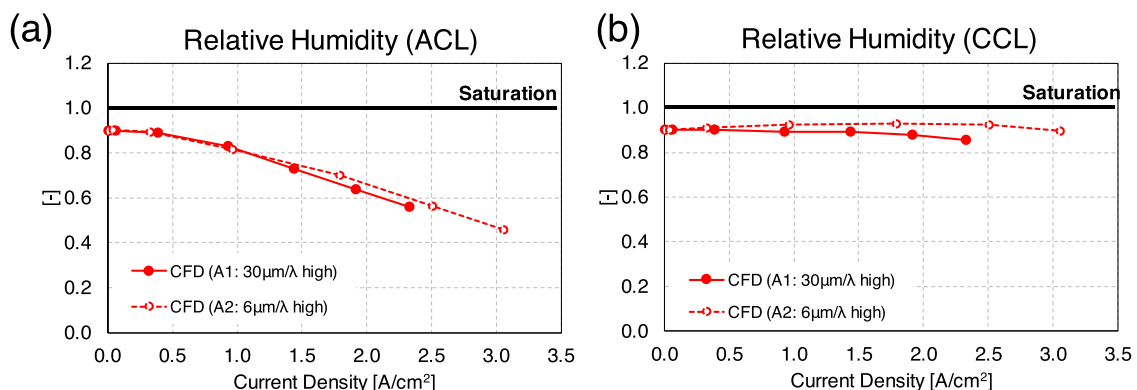


Fig. 5. Average relative humidity at (a) ACL and at (b) CCL for the A1 and A2 cells at test conditions from simulation results.

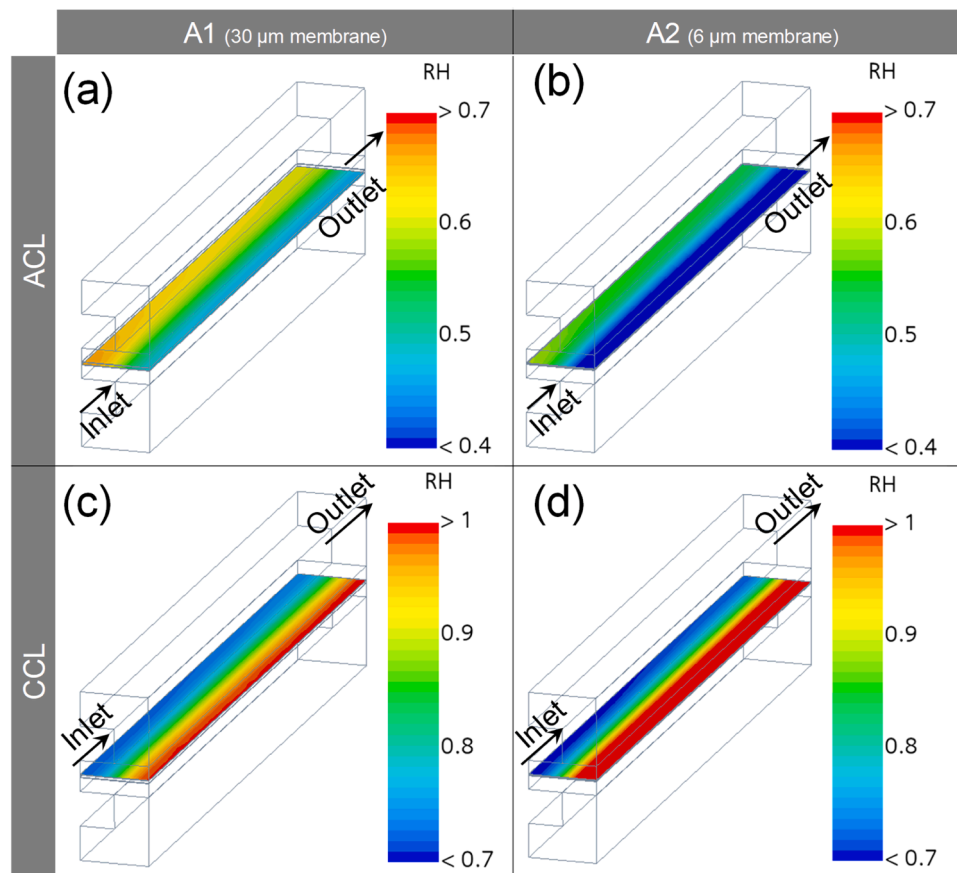


Fig. 6. Simulated RH spatial distribution for the A1 (left column, a-c) and A2 (right column, b-d) cases at 0.4 V, at ACL (top row, a-b) and CCL (bottom row, c-d).

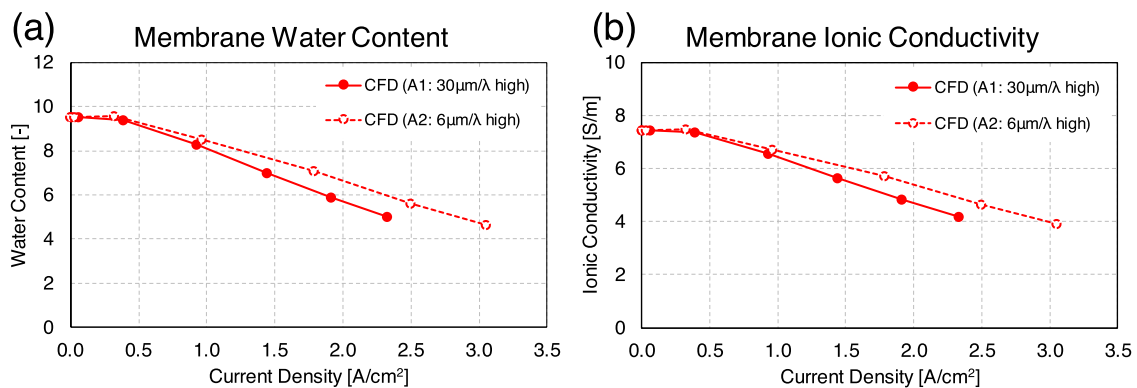


Fig. 7. (a) Average membrane water content and (b) average membrane ionic conductivity for the A1/A2 cells at test conditions from simulation results.

each membrane, as well as those with the most acute de-hydration entity at ACL, with local minima as low as $RH=0.4$ under the bipolar plate ribs (Fig. 6-a/b). Conversely, a specular RH distribution is observed at CCL (Fig. 6-c/d), with local maxima under the bipolar plate ribs due to the concurrent water generation and oxygen depletion, creating a locally water-rich gaseous mixture.

The local membrane water content depends on the RH both at ACL and at CCL as per Eq. (18), and the average water content reported in Fig. 7-a confirms its reduction for increasing current density, which remains less critical for A2 than for A1 cases. The ionic conductivity is calculated as in Eq. (21), and the average value is reported in Fig. 7-b, following the trend indicated by the average water content and confirming a generally less conductive electrolyte under high current density operation, with the thin membrane cases (A2) maintaining both a

higher humidification and conductivity with respect to the thick membrane ones (A1). It is important to underline that the ionic conductivity is a material property, i.e. per unit thickness, and that does not directly depend on the membrane thickness, thus being a size-independent material variable.

Finally, the water phase transition is observed at ACL and CCL. At ACL the de-hydration process leads to ubiquitous undersaturated conditions, hence the admitted gaseous mixture is not involved in phase transition, whereas at CCL a more complex situation arises. Locally water-rich conditions originate under the bipolar plate ribs, due to the water accumulation from the high electrochemical reaction rate and to cathodic-oriented EOD transport. Hence, the saturation limit is locally overcome, and a condensation process is initiated. This consists in a gas-to-liquid mass transfer rate, modelled as in Eq. (12), and in a

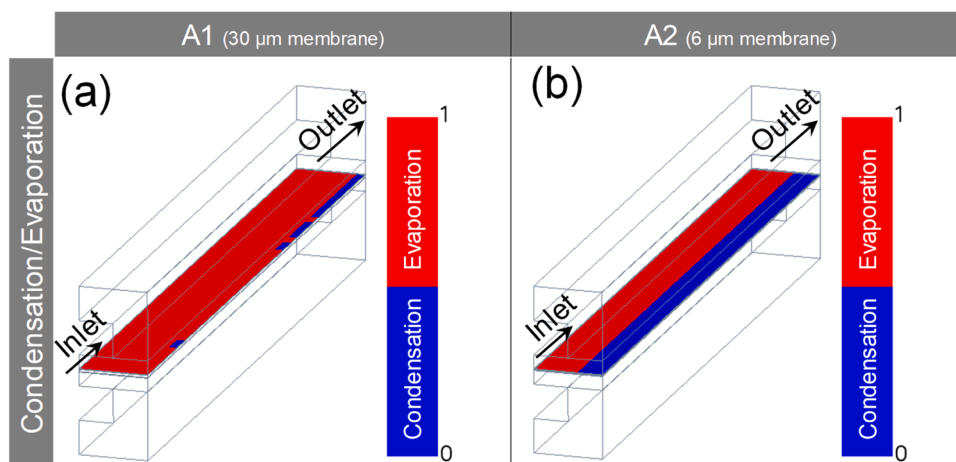


Fig. 8. Simulated condensation/evaporation condition for the A1 (left column, a) and A2 (right column, b) cases at 0.4 V at CCL.

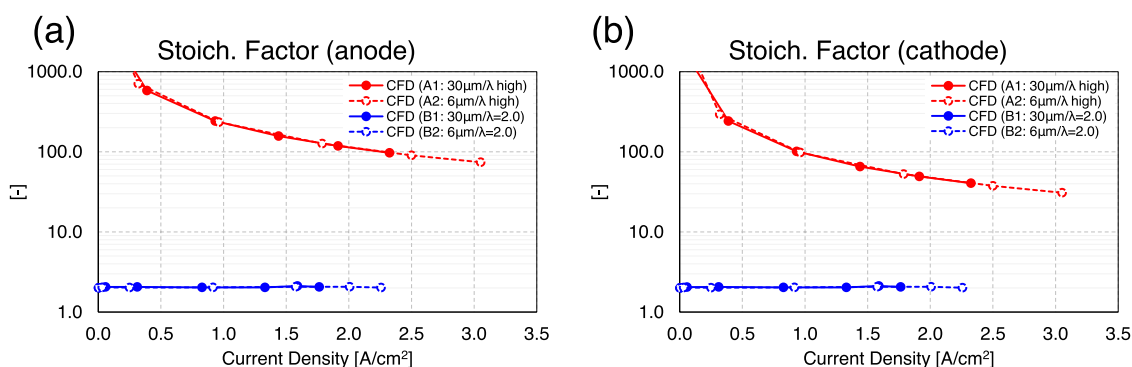


Fig. 9. Stoichiometric factors at anode (a) and cathode (b) for the high stoichiometry cases (A1, A2) and for the low stoichiometry ones (B1, B2).

condensation heat source, as in Eq. (13). In Fig. 8a local binary (0/1) indicator or the condensation/evaporation condition at CCL is reported for the 0.4 V cases, clearly showing that condensation loci are always localized under the bipolar plate ribs, and that the A2 case ($i = 3.05 \text{ A cm}^{-2}$) is much more subject to intense condensation than the A1 one ($i = 2.33 \text{ A cm}^{-2}$), due to the increased water production rate associated to the higher current density.

4.2. Results at low stoichiometry

The high flow rate in [6] used for the validation study are explicitly applied to maximize the reactants mass transport rate, hence to promote the uniformity of mass, heat and charge transport on the entire MEA surface. However, such operations are far from the conditions of

practical interest, where low stoichiometric values are necessary to limit the parasitic power losses [37,38]. Therefore, an iterative closed-loop algorithm is in-house implemented to modify the inlet flow rate based on the error between the obtained $\lambda_{a/c}$ and the target value ($\lambda_{a/c} = 2.0$), until convergence is met. In Fig. 9 the $\lambda_{a/c}$ values are calculated for the A1/A2 cases ($\lambda_{a/c} > 30$) and for B1/B2 ones, confirming that the $\lambda_{a/c} = 2.0$ condition is met within an acceptable $\Delta\lambda_{a/c} = \pm 0.1$ tolerance. Despite the absence of experimental data available for such conditions, the presented analysis is based on the same governing equations and conservation principles outlined in Section 2 without model variations, hence it is considered a physics-based simulation framework to infer the interplay of transport processes under a different reactants' flow rate and understand how these are affected by a different separator

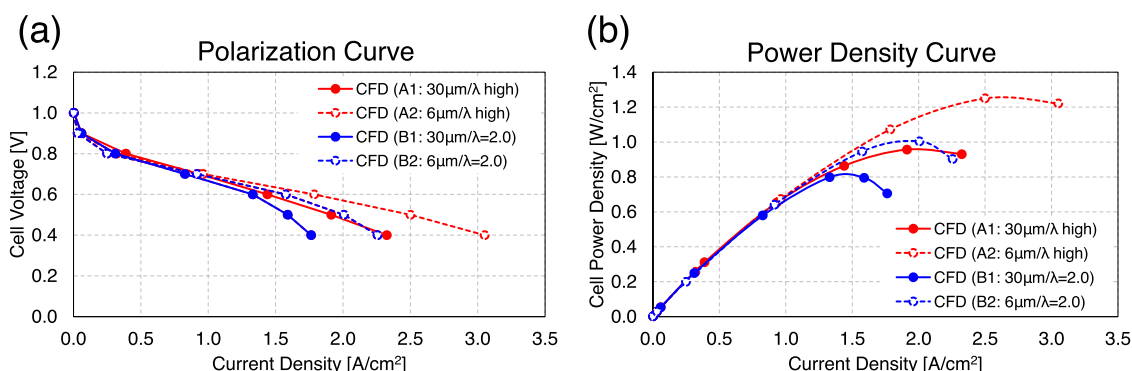


Fig. 10. (a) Polarization curves and (b) power density curves for the B1/B2 cells ($\lambda_{a/c} = 2.0$, blue), compared with A1/A2 cells at high stoichiometry (red).

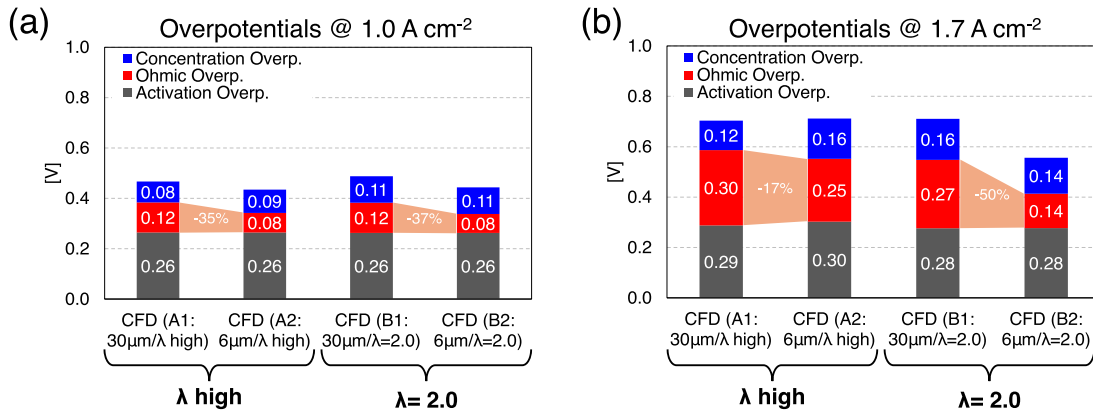


Fig. 11. Overpotentials breakdown: activation (grey), ohmic (red) and concentration (blue) for the four simulated cases (high stoichiometry: A1/A2, low stoichiometry: B1/B2), at (a) medium (1.0 A cm^{-2}) and (b) high current density (1.7 A cm^{-2}).

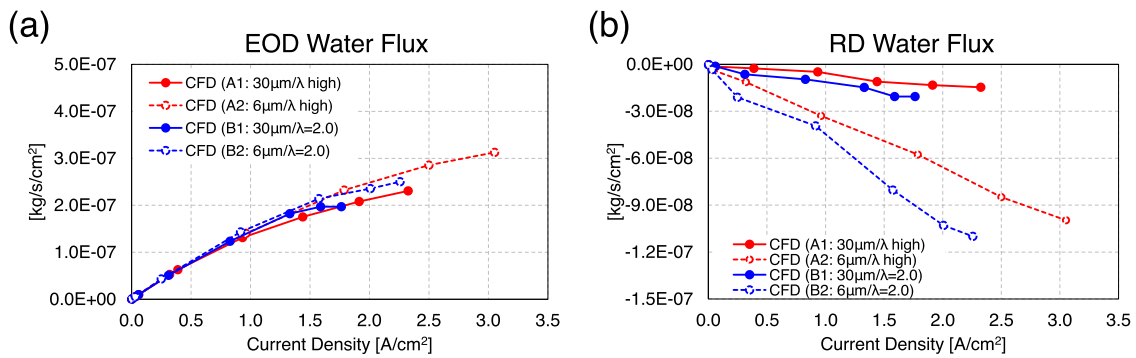


Fig. 12. Mass fluxes at CCL due to (a) EOD and (b) RD for the A1/A2 cells (high stoichiometry, red) and B1/B2 cells (low stoichiometry, blue). Thick membrane ($30 \mu\text{m}$) cases in solid line (A1, B1), thin membrane ($6 \mu\text{m}$) cases in dashed line (A2, B2).

thickness.

The polarization and power density (P'' [W m^{-2}]) curves for the B1/B2 cases are reported in Fig. 10-a/b, alongside the counterparts at high stoichiometric factor (A1/A2 series), for the sake of comparison. As visible, while the thin membrane case (B2) confirms the lower ohmic losses than the thick membrane one (B1) also under low flow rates, both suffer a relevant overpotential increase with respect to their high stoichiometry counterparts (A2 and A1, respectively).

Hence, the comparison of the four series (high/low stoichiometry, thick/thin membrane) focuses on overpotentials breakdown, and in Fig. 11 the activation, ohmic and concentration overpotentials are reported for the four series at medium (1.0 A cm^{-2}) and high current density (1.7 A cm^{-2}). It is evident that the introduction of thin membranes mainly affects the ohmic overpotential, as visible in the A1/A2 and B1/B2 comparisons, whereas both the activation and the concentration overpotentials are almost invaried. However, it is interesting to note that whereas at 1.0 A cm^{-2} a similar reduction is observed (-35% and -37% , respectively) under all the stoichiometric ratios (Fig. 11-a), at 1.7 A cm^{-2} such reduction is amplified for the low stoichiometric ratio cases (Fig. 11-b), moving from -17% for the cases at test conditions (high $\lambda_{a/c}$) to -50% for the $\lambda_{a/c} = 2.0$ cases. Therefore, this indicates a higher-than-expected relevance to the use of thin membranes under realistic stoichiometry, suggesting a better hydration state for the ultrathin membrane case (B2), whose entity would be underestimated if only test conditions at high $\lambda_{a/c}$ were observed. In the next section, the effects of membrane thickness on water balance and self-humidification characteristics will be analysed to motivate such aspect.

4.3. Membrane water balance analysis

The analysis of the membrane water management is carried out considering the combined effect of the electro-osmotic drag and of the retro-diffusion (RD) on water transport. The EOD flux is uniquely directed towards the cathode, as it shares the cationic migration in the acid electrolyte, whereas liquid water diffusion is generally oriented towards the negative gradient of species concentration. However, being the CCL typically at higher liquid water concentration than ACL, an anodic-oriented flux originates, hence the “retro-diffusion” name. The vapor water diffusion will be treated in the next section dealing with the gas species crossover. The analysis of fluxes is preferred over the mass flow rate to provide a size-independent metric (i.e., per unit surface).

The resulting EOD and RD mass fluxes (\dot{m}_{EOD} and \dot{m}_{RD} [$\text{kg m}^{-2} \text{ s}^{-1}$], respectively) are reported in Fig. 12-a/b for all cases, conventionally observed at CCL (mass addition/removal for positive/negative mass flux, respectively). The results show that:

- \dot{m}_{EOD} generally follows an increasing trend with the current density, coherently with Eq. (15), although a less-than-linear tendency is observed due to the n_d reduction with membrane dehydration (Fig. 7).
- \dot{m}_{EOD} is almost insensitive to membrane thickness and cell stoichiometry, as all simulation results show similar EOD fluxes for a given current density.
- \dot{m}_{RD} at CCL is always negative, confirming the anodic-oriented liquid water diffusion, and its magnitude is inversely proportional to the membrane thickness, i.e., higher for thin membrane cases (A2, B2) than for their thick membrane counterparts (A1, B1). Focusing on the stoichiometric factor, a more intense \dot{m}_{RD} is observed for low

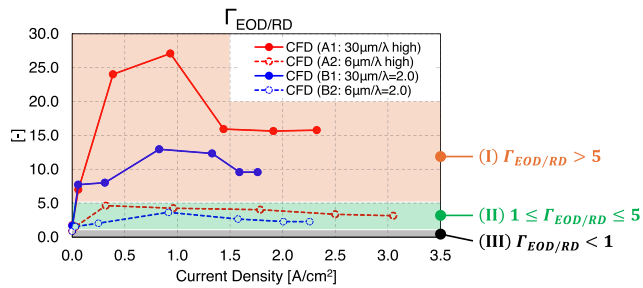


Fig. 13. $\Gamma_{EOD/RD}$ index for the A1/A2 cells (high stoichiometry, red) and B1/B2 cells (low stoichiometry, blue). Thick membrane (30 μm) cases in solid line (A1, B1), thin membrane (6 μm) cases in dashed line (A2, B2).

stoichiometry operation (B1, B2), indicating a combined effect of reduced flow rate and ultra-thin membrane for maximum retrodiffusion, which is key to self-humidification.

The \dot{m}_{EOD} and \dot{m}_{RD} contributions are rationalized to define a Figure of Merit (FoM) ($\Gamma_{EOD/RD}$, Eq. (29)), expressing the “MEA dominant transport index” as the ratio of the EOD and RD mass fluxes, respectively (Eq. (15), 22, 24), and quantifying the level of EOD dominance ($\Gamma_{EOD/RD} > 1$), the opposite condition ($\Gamma_{EOD/RD} < 1$), or an equilibrated self-humidification condition ($\Gamma_{EOD/RD} = 1.0$). In this analysis the ratio of mass fluxes is preferred over their algebraic sum (e.g., net water flux) to define a non-dimensional metric. For the sake of clarity, the absolute value of \dot{m}_{RD} is considered, to draw magnitude-based considerations on EOD and RD mass transport.

$$\Gamma_{EOD/RD} = \frac{\dot{m}_{EOD}}{|\dot{m}_{RD}|} \quad (29)$$

The obtained $\Gamma_{EOD/RD}$ results are resumed in Fig. 13, outlining three scenarios which will be related to the produced power density and to grade its external humidifying request:

- I. $\Gamma_{EOD/RD} > 5$: MEA condition with $\dot{m}_{EOD} > 5 |\dot{m}_{RD}|$, hence with a cathodic-oriented EOD water flux largely dominating on the anodic-oriented RD (i.e., >5 times larger), with a high demand of external water supply to avoid ACL dehydration (e.g., from humidifiers) and a poor self-humidification quality.
- II. $1 \leq \Gamma_{EOD/RD} \leq 5$: MEA condition with a dominance of \dot{m}_{EOD} , but where the \dot{m}_{RD} contribution to self-humidification is considerable, defining a design with an appreciable passive humidification level, i.e., relying on internal water recirculation with a reduced need for external water supply. Although the $\Gamma_{EOD/RD} = 1.0$ condition would be desirable, this range of $\Gamma_{EOD/RD}$ is a more

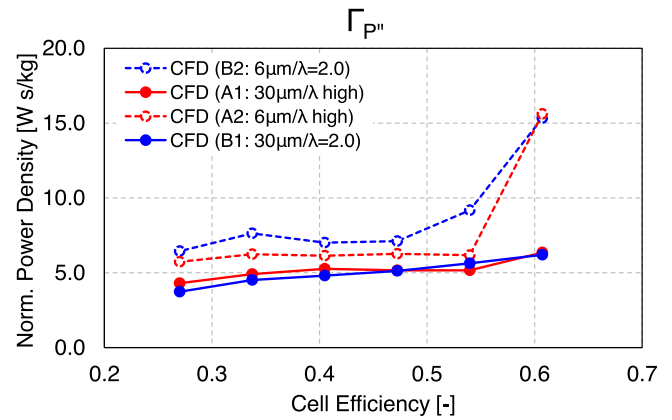


Fig. 15. Self-humidification quality metric ($\Gamma_{P'}$) as a function of the cell's thermodynamic efficiency (HHV based) for the A1/A2 cells (high stoichiometry, red) and B1/B2 cells (low stoichiometry, blue). Thick membrane (30 μm) cases in solid line (A1, B1), thin membrane (6 μm) cases in dashed line (A2, B2).

achievable target, hence of high interest in view of its good self-humidification quality.

- III. $\Gamma_{EOD/RD} < 1$: a less common condition, where the anodic-oriented \dot{m}_{RD} overcomes the cathodic-oriented \dot{m}_{EOD} , requiring an external water supply from humidifiers to avoid ACL dehydration.

The analysis of the $\Gamma_{EOD/RD}$ function in Fig. 13 shows that thick membrane cases (A1, B1, solid lines) are in the $\Gamma_{EOD/RD} > 5$ condition (Case I), with a dominance of EOD over RD and a high request of externally supplied water, although this is less severe under realistic stoichiometry (B1, with maximum $\Gamma_{EOD/RD} = 13.0$) than for test ones (A1, with maximum $\Gamma_{EOD/RD} = 27.1$). Moving to thin membrane cases (A2, B2, dashed lines), the $1 \leq \Gamma_{EOD/RD} \leq 5$ condition (Case II) is satisfied for both test and realistic stoichiometries, again with lower $\Gamma_{EOD/RD}$ values for the latter. These results indicate the quality of thin membrane MEAs in reducing the need of external water supply thanks to the promotion of internally recirculated water for humidification purposes. As illustrated in Fig. 14, the lower ohmic losses unambiguously enhance the cell's specific performance. This can be applied either to increase the power density at constant efficiency, or to improve the efficiency at constant power density. The former approach is exemplified in the B1 case at 0.5 V (Fig. 14-b), where the adoption of a thin membrane (B2) leads to a higher power density (+26.2 % at equal $\eta_c=0.34$) or efficiency (+30.4 % at equal power density of 0.79 W cm^{-2}). Finally, the RD-dominant condition (Case III) is never observed in the simulation results.

This is further elucidated by the analysis of a second FoM where the power density is rationalized on the net water flux ($\Gamma_{P'}$ [W s kg^{-1}], Eq. (30)), with \dot{m}_{net} calculated as in Eq. (28). As this FoM quantifies the

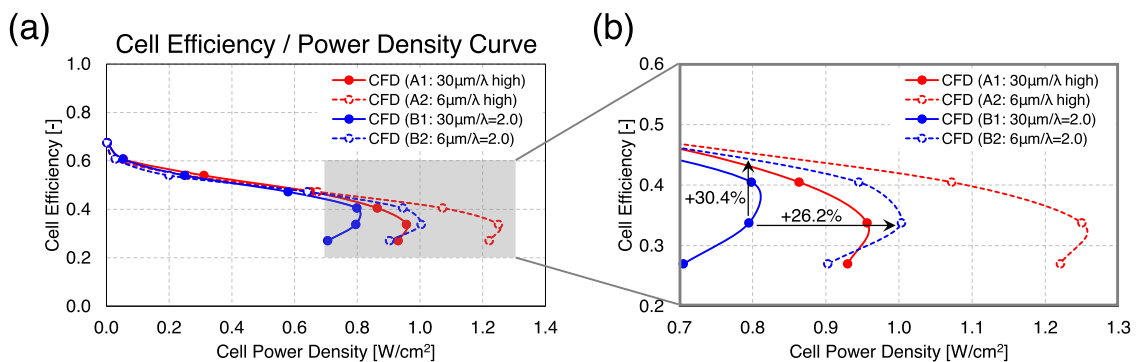


Fig. 14. (a) Cell efficiency as a function of the power density, and (b) close-up on the high power density region, for the A1/A2 cells (high stoichiometry, red) and B1/B2 cells (low stoichiometry, blue). Thick membrane (30 μm) cases in solid line (A1, B1), thin membrane (6 μm) cases in dashed line (A2, B2).

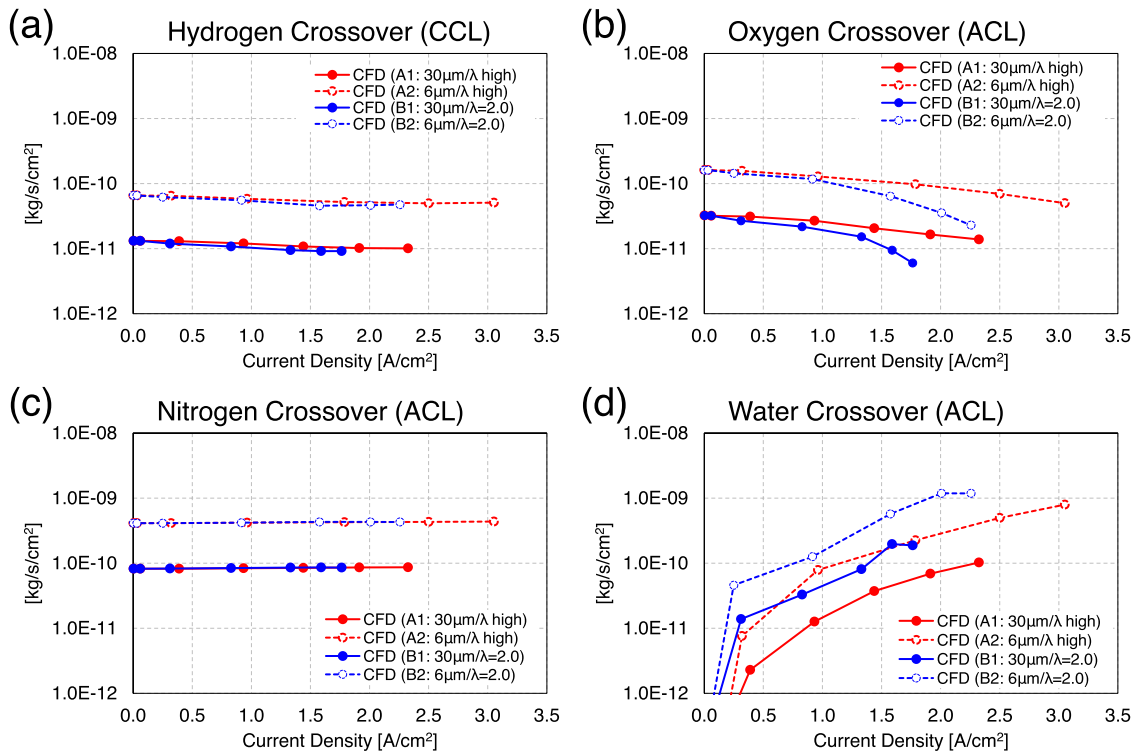


Fig. 16. Species crossover mass fluxes for (a) hydrogen at CCL, (b) oxygen at ACL, (c) nitrogen at ACL, and (d) water vapour at ACL, for the A1/A2 cells (high stoichiometry, red) and B1/B2 cells (low stoichiometry, blue). Thick membrane (30 μm) cases in solid line (A1, B1), thin membrane (6 μm) cases in dashed line (A2, B2).

relationship between the produced power density and the net water flux (Eq. 31), it is used to isolate the electric power density production from the underlying net water flux, introducing the concept of “self-humidification quality of the power density”.

$$\Gamma_{p^*} = \frac{P^*}{\dot{m}_{net}} \quad (30)$$

$$\dot{m}_{net} = \dot{m}_{EOD} + \dot{m}_{RD} \quad (31)$$

In Fig. 15 the Γ_{p^*} values for all cases are reported as a function of the cell's thermodynamic efficiency, calculated as the ratio of the cell voltage over the HHV (Higher Heating Value) thermoneutral potential, to draw conclusions not affected by efficiency variations. The results show that for all the efficiency range, an increase in the Γ_{p^*} index is obtained reducing the membrane thickness under the same stoichiometry (i.e., solid-to-dashed series in Fig. 15), meaning that a higher power density is obtained per unit of net water flux, under the same operating efficiency. This depicts an electric power generation more reliant on internal self-humidification, i.e. having a higher self-humidification degree (Γ_{p^*}) and confirming the better hydration quality hypothesized in [11]. The effect is amplified when moving from high stoichiometry cases to low ones (i.e., red-to-blue series in Fig. 15), further emphasizing the relevance of this process under realistic operation. This demonstrates the primary relevance of thin membranes in the development process of high power density and high-efficiency PEMFCs, indicating a design path to generate a self-humidification attribute to the generated power.

4.4. Gas Crossover at high and low stoichiometry

The crossover effects of gas species are modelled using Eqs. (22) and 24 for H_2 , O_2 , N_2 and for water vapour. The resulting mass fluxes across the MEA are reported in Fig. 16, observed at CCL or at ACL depending on their positive sign as required for the logarithmic y-scale. Starting from

H_2 crossover (Fig. 16-a), a CCL-oriented flux is present under all conditions, strongly depending on the membrane thickness and being emphasized for thin membranes. A similar trend is observed for O_2 (Fig. 16-b), where an ACL-oriented flux is present and whose magnitude is amplified for thin membranes. However, the O_2 crossover flux clearly shows the effect of low stoichiometry for the B1-B2 cases, exhibiting a flux reduction due to oxygen starvation at CCL under high current density, ultimately reducing the concentration gradient necessary for the crossover flux. The ACL-directed crossover flux of N_2 (Fig. 16-c) is independent of the reaction rate and inversely proportional to membrane thickness. Finally, the water vapour crossover flux (Fig. 16-d) is the one most dependent on the reaction rate, via the electrochemical production rate of water at CCL that creates the concentration gradient. The water vapour crossover flux increases both with thin membranes, as expected, and at high current densities, peaking around $1.0 \times 10^{-9} \text{ kg s}^{-1} \text{ cm}^{-2}$ and representing the highest crossover flux contribution. This, together with the ACL-directed N_2 flux, poses a research focus on the flux of the cathodic species (water vapour and nitrogen) towards the anode, and these results will be used in future modelling studies to numerically study the transport of these undesired species away from ACL.

5. Conclusions

The necessity to enhance the power of PEMFCs and to lower their specific cost to advance their contribution to decarbonization is pursued via the use of ultra-thin membranes and by strategies to promote self-humidification. The interconnection of both development directions requires a comprehensive analysis of both the electric performance and the associated water management, with an interplay of processes that differs from the high flow rate conditions (typical of laboratory testing) to realistic low flow rates. While it is known that ultra-thin membranes reduce the ohmic losses, the related variations in the membrane water management and species crossover are less investigated, preventing a

comprehensive understanding their potential and limitations. This is made even more challenging by the absence of quantitative indices to grade the dominant water transport mode across the membrane and the self-humidification degree. The key outcomes from this study are:

- A numerical model using the STAR-CCM+ CFD code is carried out on a literature experimental data from [6], where two membrane thicknesses (30 and 6 μm) were tested under high flow rates. The model includes an in-house developed sub-model for through-membrane fluxes.
- Simulations are numerically extended to more realistic values ($\lambda_{a/c} = 2.0$), observing that the relevance of ultra-thin membranes is amplified under low stoichiometry and high current density.
- A *MEA dominant transport index* ($\Gamma_{EOD/RD}$) is proposed, identifying the dominant water transport mode across the membrane. The results indicate that ultra-thin membranes allow a good self-humidification quality, which excels for the operation at low stoichiometry ($1 \leq \Gamma_{EOD/RD} \leq 5$).
- A *Self-humidification index of the power density* (Γ_{P^-}) is introduced, rationalizing the produced power density to the net water flux. Results show an increase in the Γ_{P^-} index for ultra-thin membrane cases, stating that a higher power density is obtained per unit of net water flux.
- The most relevant species crossover fluxes are the anodic-directed ones, namely N_2 and water vapor, whose entity is maximized for ultra-thin membranes.

The study reveals the complexity of the interconnected electrical operation and water management for various membrane thicknesses and flow rates, and it reveals that the ultra-thin membrane operation not only leads to a cell resistance reduction, but it extends to (i) a more self-humidified membrane and (ii) a reduced request on the humidification system under the same performance, although (iii) at the cost of higher anodic N_2 and water vapour. The two original Figures of Merit proposed from this analysis can be adopted to meter the membrane hydration state and to grade new cell designs aiming at complete self-humidification, contributing to the advancement of PEMFC design methods for large-scale industry requirements.

CRedit authorship contribution statement

Alessandro d'Adamo: Writing – original draft, Supervision, Methodology, Investigation, Funding acquisition, Formal analysis, Conceptualization, Project administration. **Lorenzo Martocchia:** Writing – review & editing, Methodology, Investigation, Formal analysis, Software. **Federico Croci:** Writing – review & editing, Methodology, Investigation, Formal analysis, Software. **Carmine Marra:** Writing – review & editing, Methodology, Data curation, Formal analysis.

Declaration of competing interest

The authors declare the following financial interests/personal relationships which may be considered as potential competing interests:

Alessandro d'Adamo reports financial support was provided by University of Modena and Reggio Emilia Department of Engineering Enzo Ferrari. Lorenzo Martocchia reports financial support was provided by Emilia-Romagna Region. Federico Croci reports financial support was provided by European Union. Carmine Marra reports financial support was provided by European Union. If there are other authors, they declare that they have no known competing financial interests or personal relationships that could have appeared to influence the work reported in this paper.

Acknowledgement

Alessandro d'Adamo acknowledges the funding granted by the Dipartimento di Ingegneria “Enzo Ferrari”, Università degli Studi di Modena e Reggio Emilia (Italy), through the project FARD (Fondo di Ateneoper la Ricerca Dipartimentale) 2024–25.

Lorenzo Martocchia acknowledges the financial support provided by Regione Emilia-Romagna (Italy), Borsa di Dottorato (39° Ciclo RIF. PA 2023-19066/RER– Codice CUP: E83C23000510002).

Federico Croci and Carmine Marra acknowledge the financial support provided by European Union, NextGenerationEU for PhD Scholarship funding at Dipartimento di Ingegneria “Enzo Ferrari” (Università degli Studi di Modena e Reggio Emilia, Italy), CUP: E93C23001710008, Corso: DOT1317193 - INGEGNERIA MECCANICA E DEL VEICOLO.

Data availability

Data will be made available on request.

References

- [1] “World energy outlook 2024 – analysis - IEA.” Accessed: Dec. 03, 2024. [Online]. Available: <https://www.iea.org/reports/world-energy-outlook-2024>, 2024.
- [2] “The role of E-fuels in decarbonising transport – analysis - IEA.” Accessed: Dec. 03, 2024. [Online]. Available: <https://www.iea.org/reports/the-role-of-e-fuels-in-decarbonising-transport>, 2024.
- [3] J.M. Andújar, F. Segura, J. Rey, F.J. Vivas, Batteries and hydrogen storage: technical analysis and commercial revision to select the best option, *Energies* 15 (17) (Aug. 2022) 6196, <https://doi.org/10.3390/EN15176196>, 2022, Vol. 15, Page 6196.
- [4] A. Ajanovic, R. Haas, Economic and environmental prospects for battery electric and fuel cell vehicles: a review, *Fuel Cells* 19 (5) (Oct. 2019) 515–529, <https://doi.org/10.1002/FUCE.201800171>.
- [5] “Global hydrogen Review 2024 – analysis - IEA.” Accessed: Dec. 03, 2024. [Online]. Available: <https://www.iea.org/reports/global-hydrogen-review-2024>, 2024.
- [6] Y. Tabuchi, T. Shiomi, O. Aoki, N. Kubo, K. Shinohara, Effects of heat and water transport on the performance of polymer electrolyte membrane fuel cell under high current density operation, *Electrochim. Acta.* 56 (1) (Dec. 2010) 352–360, <https://doi.org/10.1016/J.ELECTACTA.2010.08.070>.
- [7] T. Yoshizumi, H. Kubo, M. Okumura, Development of high-performance FC stack for the new MIRAL, *SAE Tech. Papers* (2021) (Apr. 2021), <https://doi.org/10.4271/2021-01-0740>.
- [8] K.H. Wong, E. Kjeang, Macroscopic In-situ modeling of chemical membrane degradation in polymer electrolyte fuel cells, *J. Electrochem. Soc.* 161 (9) (May 2014) F823–F832, <https://doi.org/10.1149/2.0031409JES/XML>.
- [9] B. Kienitz, Optimizing polymer electrolyte membrane thickness to maximize fuel cell vehicle range, *Int. J. Hydrogen Energy* 46 (19) (Mar. 2021) 11176–11182, <https://doi.org/10.1016/J.IJHYDENE.2020.03.126>.
- [10] C.Y. Jung, T.H. Kim, S.C. Yi, Ultrahigh PEMFC performance of a thin-film, dual-electrode assembly with tailored electrode morphology, *ChemSusChem* 7 (2) (Feb. 2014) 466–473, <https://doi.org/10.1002/SSC.201301043>.
- [11] B. Kienitz, J. Kolde, S. Priester, C. Baczkowski, M. Crum, Ultra-thin reinforced ionomer membranes to meet next generation fuel cell targets, *ECS Trans.* 41 (1) (Oct. 2011) 1521–1530, <https://doi.org/10.1149/1.3635683/XML>.
- [12] W. Liu, T. Suzuki, H. Mao, T. Schmiedel, Development of thin, reinforced PEMFC membranes through understanding of structure-property-performance relationships, *ECS Trans.* 50 (2) (Mar. 2013) 51–64, <https://doi.org/10.1149/05002.0051ECST/XML>.
- [13] A. D'Adamo, M. Haslinger, G. Corda, J. Höflinger, S. Fontanesi, T. Lauer, Modelling methods and validation techniques for CFD simulations of PEM fuel cells, *Processes* 9 (4) (Apr. 2021) 688, <https://doi.org/10.3390/PR9040688>, 2021, Vol. 9, Page 688.
- [14] K. Jiao, X. Li, Water transport in polymer electrolyte membrane fuel cells, *Prog. Energy Combust. Sci.* 37 (3) (Jun. 2011) 221–291, <https://doi.org/10.1016/J.PECS.2010.06.002>.
- [15] C.Y. Wang, Fundamental models for fuel cell engineering, *Chem. Rev.* 104 (10) (Oct. 2004) 4727–4765, <https://doi.org/10.1021/CR020718S>.
- [16] H. Wu, X. Li, P. Berg, On the modeling of water transport in polymer electrolyte membrane fuel cells, *Electrochim. Acta.* 54 (27) (Nov. 2009) 6913–6927, <https://doi.org/10.1016/J.ELECTACTA.2009.06.070>.
- [17] A.R. Sangtabi, A. Kianifar, E. Alizadeh, Effect of water vapor condensation on the flow distribution in a PEM fuel cell stack, *Int. J. Heat Mass Transf.* 151 (Apr. 2020) 119471, <https://doi.org/10.1016/J.IJHEATMASSTRANSFER.2020.119471>.
- [18] T.E. Springer, T.A. Zawodzinski, S. Gottesfeld, Polymer electrolyte fuel cell model, *J. Electrochem. Soc.* 138 (8) (Aug. 1991) 2334–2342, <https://doi.org/10.1149/1.2085971/XML>.
- [19] A.Z. Weber, J. Newman, Transport in polymer-electrolyte membranes: I. Physical model, *J. Electrochem. Soc.* 150 (7) (Jun. 2003) A1008, <https://doi.org/10.1149/1.1580822>.

- [20] A.Z. Weber, J. Newman, Transport in polymer-electrolyte membranes : II. Mathematical model, *J. Electrochem. Soc.* 151 (2) (Jan. 2004) A311, <https://doi.org/10.1149/1.1639157>.
- [21] A.Z. Weber, J. Newman, Transport in polymer-electrolyte membranes : III. Model validation in a simple fuel-cell model, *J. Electrochem. Soc.* 151 (2) (Jan. 2004) A326, <https://doi.org/10.1149/1.1639158>.
- [22] D.M. Bernardi, M.W. Verbrugge, A mathematical model of the solid-polymer-electrolyte fuel cell, *J. Electrochem. Soc.* 139 (9) (Sep. 1992) 2477–2491, <https://doi.org/10.1149/1.2221251>.
- [23] S.S. Kocha, J.D. Yang, J.S. Yi, Characterization of gas crossover and its implications in PEM fuel cells, *AIChE J.* 52 (5) (May 2006) 1916–1925, <https://doi.org/10.1002/AIC.10780>.
- [24] X. Cheng, et al., Hydrogen crossover in high-temperature PEM fuel cells, *J. Power Sources* 167 (1) (May 2007) 25–31, <https://doi.org/10.1016/j.jpowsour.2007.02.027>.
- [25] M. Schoemaker, U. Misz, P. Beckhaus, A. Heinzl, Evaluation of hydrogen crossover through fuel cell membranes, *Fuel Cells* 14 (3) (Jun. 2014) 412–415, <https://doi.org/10.1002/fuce.201300215>.
- [26] K.D. Baik, M.S. Kim, Characterization of nitrogen gas crossover through the membrane in proton-exchange membrane fuel cells, *Int. J. Hydrogen Energy* 36 (1) (Jan. 2011) 732–739, <https://doi.org/10.1016/J.IJHYDENE.2010.09.046>.
- [27] M.M. Mench, Fuel cell engines, *Fuel Cell Engines* (Apr. 2008) 1–515, <https://doi.org/10.1002/9780470209769>.
- [28] S. Motupally, A.J. Becker, J.W. Weidner, Diffusion of water in Nafion 115 membranes, *J. Electrochem. Soc.* 147 (9) (Sep. 2000) 3171, <https://doi.org/10.1149/1.1393879/XML>.
- [29] R.K. Ahluwalia, X. Wang, Buildup of nitrogen in direct hydrogen polymer-electrolyte fuel cell stacks, *J. Power Sources* 171 (1) (Sep. 2007) 63–71, <https://doi.org/10.1016/J.JPOWSOUR.2007.01.032>.
- [30] A. D'Adamo, M. Riccardi, C. Locci, M. Romagnoli, S. Fontanesi, Numerical simulation of a high current density PEM fuel cell, *SAE Tech. Papers* (2020) (Sep. 2020), <https://doi.org/10.4271/2020-24-0016>.
- [31] G. Corda, S. Fontanesi, A. d'Adamo, Methodology for PEMFC CFD simulation including the effect of porous parts compression, *Int. J. Hydrogen Energy* (Mar. 2022), <https://doi.org/10.1016/J.IJHYDENE.2022.02.201>.
- [32] A. D'Adamo, et al., CFD simulations and potential of nanofluids for PEM fuel cells cooling, *SAE Tech. Papers* (Aug. 2023), <https://doi.org/10.4271/2023-24-0144>.
- [33] A. D'Adamo, G. Corda, Numerical simulation of advanced bipolar plates materials for hydrogen-fueled PEM fuel cell, *SAE Tech. Papers* (2022) (Mar. 2022), <https://doi.org/10.4271/2022-01-0683>.
- [34] G. Corda, S. Fontanesi, A. D'Adamo, Numerical comparison of the performance of four cooling circuit designs for proton exchange membrane fuel cells (PEMFCs), *SAE Tech. Papers* (2022) (Mar. 2022), <https://doi.org/10.4271/2022-01-0685>.
- [35] J.T. Gostick, M.W. Fowler, M.D. Pritzker, M.A. Ioannidis, L.M. Behra, In-plane and through-plane gas permeability of carbon fiber electrode backing layers, *J. Power Sources* 162 (1) (Nov. 2006) 228–238, <https://doi.org/10.1016/J.JPOWSOUR.2006.06.096>.
- [36] T. Bednarek, G. Tsotridis, Assessment of the electrochemical characteristics of a Polymer electrolyte membrane in a reference single fuel cell testing hardware, *J. Power Sources* 473 (Oct. 2020) 228319, <https://doi.org/10.1016/J.JPOWSOUR.2020.228319>.
- [37] H. Chen, B. Liu, R. Liu, Q. Weng, T. Zhang, P. Pei, Optimal interval of air stoichiometry under different operating parameters and electrical load conditions of proton exchange membrane fuel cell, *Energy Convers. Manag.* 205 (Feb. 2020) 112398, <https://doi.org/10.1016/J.ENCONMAN.2019.112398>.
- [38] A. d'Adamo, L. Martocchia, F. Berni, S. Breda, An analytical methodology to maximize the fuel cells system efficiency using optimal cathodic pressure and flow rate, *Int. J. Hydrogen Energy* 87 (Oct. 2024) 159–170, <https://doi.org/10.1016/j.ijhydene.2024.09.018>.